Laser generated ultrasound sources using carbon-polymer nanocomposites for high frequency metrology[a)]

Srinath Rajagopal,[1, b)] Toby Sainsbury,[2, c)] Bradley E. Treeby,[3] and Ben T. Cox[3]

[1]Ultrasound and Underwater Acoustics, National Physical Laboratory, Hampton Road, Teddington, TW11 0LW, U.K.

[2]Composites, Adhesives and Polymeric Materials, National Physical Laboratory, Hampton Road, Teddington, TW11 0LW, U.K.

[3]Department of Medical Physics and Biomedical Engineering, University College London, Malet Place Engineering Building, Gower Street, London, WC1E 6BT, U.K.

Running title: Carbon-polymer nanocomposite laser-generated ultrasound sources

[a)]Portions of this work were presented in "Laser generated ultrasound sources using polymer nanocomposites for high frequency metrology," Proceedings of IEEE International Ultrasonics Symposium, Washington DC, USA, September 2017.

[b)]Electronic mail: srinath.rajagopal@npl.co.uk.

[c)]Current address: Engineering, Life Sciences and Food Division, IDA Ireland, Wilton Place, Dublin 2, Ireland.

Abstract

The characterization of ultrasound fields generated by diagnostic and therapeutic equipment is an essential requirement for performance validation and to demonstrate compliance against established safety limits. This requires hydrophones calibrated to a traceable standard. Currently, the upper calibration frequency range available to the user community is limited to 60 MHz. However, high frequencies are increasingly being used for both imaging and therapy necessitating calibration frequencies up to 100 MHz. The precise calibration of hydrophones requires a source of high amplitude, broadband, quasi-planar and stable ultrasound fields. There are challenges to using conventional piezoelectric sources, and laser generated ultrasound sources offer a promising solution. In this study, various nanocomposites consisting of a bulk polymer matrix and multi-walled carbon nanotubes were fabricated and tested using pulsed laser of few nanoseconds for their suitability as a source for high frequency calibration of hydrophones. The pressure amplitude and bandwidths were measured using a broadband hydrophone from 27 different nanocomposite sources. The effect of nonlinear propagation of high amplitude laser generated ultrasound on bandwidth and the effect of bandlimited sensitivity response on the deconvolved pressure waveform were numerically investigated. The stability of the nanocomposite sources under sustained laser pulse excitation was also examined.

I. INTRODUCTION

Miniature hydrophones manufactured using piezoelectric polyvinylidene difluoride (PVDF) polymer are the standard devices used in the characterization of fields generated by medical ultrasound equipment.[1–3] Recently, robust hydrophones based on PVDF and Fabry–Pérot ultrasound sensors have become available for the characterization of high amplitude fields generated by therapeutic ultrasound equipment.[4–7] For accurate measurements of the ultrasound fields, these devices need to be calibrated over a sufficiently wide frequency range to enable artefact-free conversion of their electrical signal to a pressure signal.[8–11] At present, the highest calibration frequency available on a routine basis is limited to 60 MHz. The calibration procedure uses a substitution method in which the responses of an unknown hydrophone and a hydrophone calibrated on the primary standard are compared in an ultrasound field under nominally identical conditions.[12–14] However, high frequency imaging applications are appearing in fields such as ophthalmology, dermatology, pediatric and peripheral vascular imaging, where frequencies in the range 40 – 70 MHz are used.[15–17] In ablative therapies and lithotripsy, low frequency (< 10 MHz) and high amplitude (tens of MPa) ultrasound waves are used to ablate tumors and break kidney stones.[18,19] The nonlinear propagation of such waves in water can generate harmonic frequency components up to 100 MHz and beyond. Therefore, a need has arisen for end users such as medical device manufacturers and academic researchers to have access to calibration data as high as 100 MHz. This will facilitate the accurate characterization required for patient safety, performance validation, and the development of new high frequency ultrasound technologies.

The primary calibration of hydrophones at most of the National Measurement Institutes, including the National Physical Laboratory (NPL), U.K., Physikalisch-Technische Bundesanstalt (PTB),

Germany, National Measurement Institute of Japan, and National Institute of Metrology, China are based on optical interferometric techniques, which measure acoustic particle displacement[20–22] or velocity[11,23] from a reflecting surface, such as a pellicle. The acoustic pressure at the optical probing location can be calculated using acoustic plane-wave relationships. The hydrophone output voltage corresponding to this acoustic pressure is then measured, and the sensitivity of the hydrophone is thereby found. The ultrasound fields currently used in such primary calibrations are linear or nonlinearly-steepened tone-burst waveforms, which provide measurement bandwidths up to 40 MHz.[24] By using focused transducer, nonlinearly-steepened short pulses (generated by spike discharge excitation of a transducer) with spectral components beyond 100 MHz has been used to calibrate hydrophones.[11,25] However, for nonlinearly-steepened fields the magnitudes of the harmonics decrease by $1/n^2$, for displacement, or $1/n$, for velocity, where n is the harmonic number. For example, if the acoustic pressure at the fundamental frequency of 5 MHz and its tenth harmonic, 50 MHz, are 500 kPa and 50 kPa, then the displacements and velocities are approximately 10.8 nm and 108 pm, and 34 $\mathrm{cm \cdot s^{-1}}$ and 3.4 $\mathrm{cm \cdot s^{-1}}$, respectively. The accuracy in the calibration of hydrophones is therefore largely limited by the ability of the interferometers to measure very small perturbations.

A calibration source that would meet most high-frequency calibration needs at present would generate an acoustic field at the measurement location that is sufficiently planar that spatial averaging errors can be ignored, have a bandwidth in excess of 100 MHz, and generate amplitudes above the noise-floor of the interferometers. Piezoelectric transducer technology is unable to meet these requirements, but photoacoustics may offer a promising solution in this regard.

In this paper, polymer nanocomposites fabricated from multi-walled carbon nanotubes dispersed in three different polymers were evaluated for their suitability as potential broadband, high amplitude and planar photoacoustic sources for application to hydrophone calibration. The manuscript is organized as follows: In Sec. II, the principles of photoacoustic wave generation are briefly discussed, a summary of literature review and a method for fabricating polymer nanocomposite sources is provided. In Sec. III, the details of the experimental setup used to measure the photoacoustic response from the polymer nanocomposites is described. In Sec. IV, the pressure amplitudes and bandwidths of the polymer nanocomposite sources are reported, and their stability under sustained laser pulse excitation is discussed. In Sec. V, the effect of nonlinear propagation on source bandwidth, as well as the bandlimited sensitivity response of the hydrophone used in the measurements are investigated using 1D numerical simulations.

II. LASER GENERATED ULTRASOUND SOURCES

A. The photoacoustic effect

When a light absorbing medium is illuminated by an optical pulse, the photons are absorbed by chromophores in the medium and the subsequent thermalization of the energy leads to simultaneous increases in temperature and pressure within the absorption volume. If the medium is elastic, and the energy deposition is sufficiently rapid, the pressure rise will propagate away as an ultrasound pulse.[26–28] For a plane wave of light incident on a medium with a constant absorption coefficient, and in the absence of scattering, the pressure rise, $p_o(z)$ is given by the Beer-Lambert-Bouguer relation:

$$p_o(z) = \Phi \mu_a \Gamma \exp(-\mu_a z), \qquad z > 0 \tag{1}$$

where Φ is the laser fluence in $\mathrm{J.\,m^{-2}}$ at the medium's surface $z = 0$, μ_a is the optical absorption coefficient in $\mathrm{m^{-1}}$, z is the perpendicular distance from the surface in m, and Γ is the dimensionless photoacoustic efficiency, or Grüneisen parameter. The Grüneisen parameter can be written in terms of other thermodynamic parameters, for example as $\Gamma = \beta c_0^2/C_p$, where β is the volume thermal expansion coefficient in $\mathrm{K^{-1}}$, c_0 is the sound-speed in $\mathrm{m \cdot s^{-1}}$ and C_p is the isobaric heat capacity in $\mathrm{J \cdot Kg^{-1} \cdot K^{-1}}$. The amplitude, bandwidth and the spatial size of the ultrasound pulse can be controlled by varying the optical pulse duration and energy, the size of the illuminated region and the physical properties of the medium.[29]

B. State-of-the-art

In photoacoustics, although coherent light is not essential, lasers are extensively used to generate the required ultrasound field because they are highly controllable and can offer the short pulse durations required. Photoacoustics in this context is therefore often referred to as Laser Generated Ultrasound (LGUS). The key findings from the literature review of LGUS sources, including pressure amplitudes and bandwidths obtained, are briefly summarized in Table I. LGUS sources were either nanocomposites made of carbon nanoparticles and polymeric materials[30–42] or fabricated gold nanoparticle arrays and films.[43–47] Carbon nanoparticles such as multi-walled carbon nanotubes, candle soot nanoparticles, carbon nanofibers, carbon black and reduced graphene oxide or gold nanoparticles, were used as light absorbers. The pressure amplitude increases with the optical absorption (see Eq. (1)), therefore, a medium with highest optical absorption will give the maximum acoustic pressure, all other things being equal. LGUS sources made of carbon nanoparticles gave higher pressure amplitudes over sources made of gold nanoparticles. Gold nanoparticles exhibit size and optical wavelength dependent resonance

absorption,[48] which is not the case for carbon nanoparticles.[49] The size distribution of gold nanoparticles in a nanocomposite and spectral purity of the excitation laser could therefore impact the LGUS pressure amplitude and bandwidth. The coefficient of volume thermal expansion of the polymer is directly proportional to the amplitude of the LGUS. Therefore, polydimethylsiloxane (PDMS), which has the highest volume thermal expansion coefficient of $340 \times 10^{-6}\ \mathrm{K}^{-1}$ has been predominantly used as the matrix material in the fabrication of nanocomposites for LGUS (see Table I).

Table I. Summary of a literature review of various photo-absorptive nanocomposite sources. MWCNT—Multi-walled carbon nanotubes, CSNP—carbon soot nanoparticles, CNF—carbon nanofibers, CB—carbon black, rGO—reduced graphene oxide, Au—gold, Al—aluminum, PDMS—polydimethylsiloxane, PMMA—polymethylmethacrylate, λ_o—laser wavelength, t_l—laser pulse duration, LGUS—laser generated ultrasound, *—indicates estimated values from the data reported within each paper.

		Photo-absorptive material		Laser parameters				LGUS pulse		
Year	Author	Type	Material disposition	λ_o [nm]	t_l [ns]	Fluence/ Energy	Spot size	Measured distance [mm]	Peak positive pressure	–6 dB bandwidth [MHz]
2017	Fan *et al*	MWCNT-PDMS	PMMA plate	532	8	120 mJ	–	10.0	6.35 MPa	< 10*
2017	Moon *et al*	MWCNT-PDMS	PMMA plate	532	8	180 mW·cm^{-2}	40 mm	10.0	3.0 MPa*	< 20*
2016	Noimark *et al*	MWCNT-PDMS	Optical fibre	1064	2	33.1 mJ·cm^{-2}	200 µm	3.00	1.36 MPa	29.2
2015	Chang *et al*	CSNP-PDMS	Glass slide	532	6	3.57 mJ·cm^{-2}	10 mm	4.20	4.8 MPa	21
2015	Hsieh *et al*	CNF-PDMS	Glass slide	532	4	3.71 mJ·cm^{-2}	12 mm	3.65	12.15 MPa	< 10*
2014	Zou *et al*	Au-PDMS	Optical fibre	532	5	8.75 mJ·cm^{-2}	200 µm	1.00	640 kPa	20
2014	Vannacci *et al*	CB film	Optical fibre	1064	0.5	50 uJ	200 µm	0.50	2.8 MPa	34*
2014	Colchester *et al*	MWCNT-PDMS	Optical fibre	1064	2	36.3 mJ·cm^{-2}	200 µm	2.00	890 kPa	15
2013	Park *et al*	rGO-Al layer	Glass slide	532	5	43 mJ·cm^{-2}	–	2.80	4.5 MPa	< 30*
2012	Lee *et al*	rGO-Al layer	Glass slide	532	5	43.28 mJ·cm^{-2}	–	2.85	7.5 MPa	20*
2007	Hou *et al*	CB-PDMS	Glass slide	1064	5	50 uJ	25 µm	10.0	800 kPa	48*

C. Source fabrication

The LGUS sources were made of nanocomposites consisting of multi-walled carbon nanotubes (MWCNT), as the light absorbing material, dispersed in a bulk polymer matrix. The optical absorption in MWCNT is the highest of any man-made material.[50] Consequently, MWCNT-based

nanocomposites have been widely tested for the laser generation of high amplitude ultrasound compared to other allotropes of carbon (see Table I). The goal of this study was to develop a LGUS source for application to the calibration of hydrophones, therefore, the stability of the source over the duration of the calibration is an important factor. The stability of PDMS-based nanocomposites under sustained pulsed laser excitation has not previously been reported. Therefore, two other polymers matrices were included in the scope of this exploratory work: i) epoxy resin – given its widespread use in industrial applications due to its high mechanical strength, thermal and chemical resistance, and ii) polyurethane – for its application as phantoms in ultrasound quality assurance measurements.

The MWCNT (Haydale Ltd, Ammanford, Carmarthenshire, U.K.) were mechanically dispersed in the polymer using a high-speed shear mixer (DAC 150.1 FV-K, SpeedMixer™, High Wycombe, U.K.). The MWCNT, polymer and catalyst (curing agent) were all combined by their mass fractions (see Table II). The MWCNT were dispersed in the polymer at 3500 rpm for 2 min followed by addition of the catalyst, and shear mixed again at 3500 rpm for 2 min. A total of 27 variations of the photo-absorptive nanocomposites (PNC) were prepared. The polymer type, weight fraction (wt%) of MWCNT in the polymer and the thickness of each of the 27 PNC sources were different. The polymer types were epoxy, polyurethane (PU) or PDMS; the three wt% of MWCNT in the polymer were 1.25, 2.5 or 3.5 wt% and the nanocomposite thicknesses were 18 – 30 μm, 40 – 60 μm or 50 – 70 μm. The MWCNT-polymer mixture was used to coat a laboratory-grade glass slide using a blade film applicator (Sheen Instruments, West Molesey, U.K). In this technique, a height adjustable knife-edged metal frame attached to a micrometer controls the gap clearance relative to a flat surface e.g., a glass slide. A thin film is produced when the excess

mixture smeared on the glass slide is removed by sliding the knife-edged metal frame over the length of the glass slide. A glass-backed PNC source was formed after oven-curing the thin film (see inset of Fig. 1). The optical absorption coefficient, μ_a, of the PNC sources were measured using a spectrophotometer (Perkin Elmer, Waltham, Massachusetts, USA) over a wavelength range of 500 to 1100 nm in 10 nm steps (see Table III). The measurements of μ_a were made on 17 – 31 μm thick PNC sources, as the thicker sources proved to be too absorbing for the spectrophotometer. The central region of the coating over an area of approximately 2×5 mm was used for the measurements. The increase in μ_a is nearly linear with wt% of MWCNT for the case of epoxy and PDMS based PNC sources but not for PU based PNC source. The nonlinear increase in μ_a for PU may have been due to nonuniform dispersion of MWCNT.

The measurements of μ_a suggest that the PNC sources should be ideally equal to optical absorption depth ($1/\mu_a$). For the case of 3.5 wt% MWCNT in PDMS the optical absorption depth estimated from the measured value of $\mu_a = 245\ \text{mm}^{-1}$(see Table III) is 4 μm. For thicknesses below 10 μm factors such as the resolution of the micrometer of the film applicator, parallelism of the glass slide and flatness of the platform on which the glass substrate was attached to lay the film affect the achievable thickness. Therefore, on a best endeavor basis PNC sources of ≈10 μm thickness were fabricated and only one sample each of epoxy, PU and PDMS based PNCs with 2.5 wt% MWCNT of ≈10 μm thickness were produced for experimental evaluation.

Table II. Polymer types employed in the preparation of photo-absorptive polymer nanocomposite sources. Mix ratios quoted in the table are for pure polymers only. To prepare the polymer nanocomposite, the mass of the base material was adjusted to accommodate the required percent weight content of MWCNT (1.25, 2.5 or 3.5 wt%).

Polymer type (Product)	**Mix ratio by weight (base:catalyst)**	**Curing conditions**
Epoxy resin (Araldite)	Araldite LY 564: 10 g Aradur 2954: 3.5 g	Oven cured for 12 hours at 70 C
Polydimethylsiloxane (SYLGARD® 184)	Elastomer: 10 g Cure accelerator: 2 g	Oven cured for 35 mins at 100 C
Polyurethane (Polycraft FC-6630)	Polyol (Part A): 5 g Isocyanate (Part B): 5 g	Oven cured for 12 hours at 40 C

Table III. The optical absorption coefficient, μ_a, of epoxy, polyurethane and polydimethylsiloxane-based PNC sources dispersed with 1.25, 2.5 and 3.5 wt% MWCNT. The quoted values represent an averaged value of measurements at 1060 and 1070 nm.

Polymer matrix	Weight content of MWCNT		
	1.25 wt%	2.50 wt%	3.50 wt%
	Optical absorption coefficient, μ_a [mm^{-1}]		
Epoxy	60	125	176
Polyurethane	47	73	216
Polydimethylsiloxane	68	167	245

III. EXPERIMENTAL PROCEDURE

A. Measurement setup

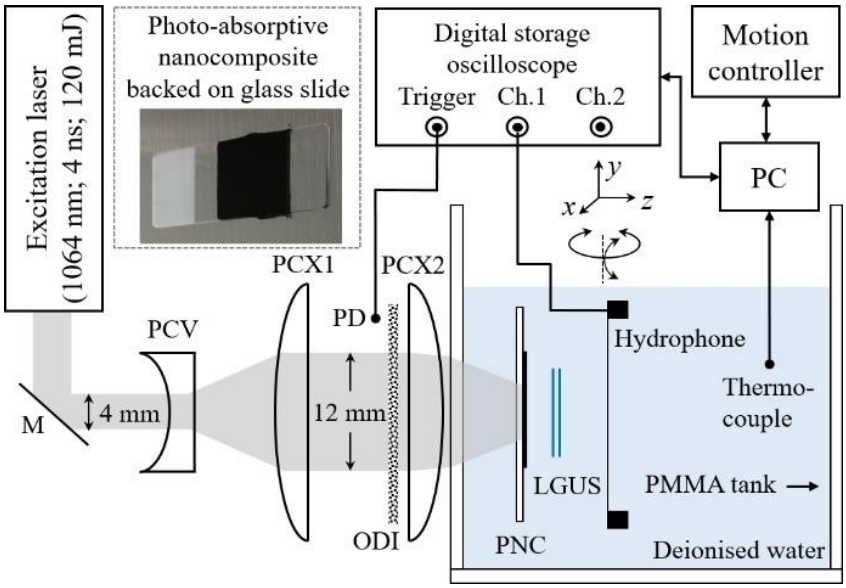

FIG. 1. (color online) The experimental setup. The inset shows a photo-absorptive nanocomposite (PNC) source backed on a glass slide. The thickness of the PNC is approximately 30 μm and was fabricated by dispersing 3.5 wt% MWCNT in epoxy. M—Mirror, PCV—plano-concave lens, PCX—plano-convex lens, PD—photodetector, ODI—optical diffuser, LGUS—laser generated ultrasound, PMMA—polymethyl methacrylate, PC—personal computer.

The test setup used to measure the LGUS responses from the PNC sources is shown in Fig. 1. A Q-switched flash lamp pumped Nd:YAG (neodymium-doped yttrium aluminum garnet) pulsed laser (Nano 120-S, Litron Ltd, U.K.) operating at 1064 nm with a full-width half-maximum of 4 ns and a peak energy of 120 mJ per pulse was used for the study. The expanded beam from the laser was homogenized using a 1500 grit ground glass optical diffuser (ODI). The homogenized beam was weakly converged using a plano-convex lens of 100 mm focal length to minimize the losses due to scatter caused by the ODI before passing through the clear polymethylmethacrylate (PMMA) wall of the water tank. A membrane hydrophone (UT1602, Precision Acoustics Ltd, UK) with a nominal element diameter of 0.2 mm was used to measure the LGUS response. A 5-axis

gantry with rotation, tilt and three motorized linear axes (LNR50S/M, Thorlabs) was used for scanning of the LGUS field from the PNC sources using ultrasound measurement software (UMS2, Precision Acoustics Ltd, Dorchester, UK). A photodetector (PD) provided a trigger to the digital oscilloscope (TDS7254, Tektronix, Beaverton, USA). The sampling rate and the record length were set to 2.5 GHz and 1250 sample points, respectively. A thermocouple placed inside the PMMA tank was used to record the water temperature. Each measurement record consisted of acquiring 32 LGUS pulses sequentially using the UT1602 hydrophone and correcting each pulse for fluctuations in the laser energy (pulse-pulse stability: 1%) using the peak voltage of the PD signal acquired simultaneously. The corrected LGUS pulses were averaged and stored for later analysis. All measurements were undertaken at an axial distance of 7.4 mm (or 5 μs time-of-flight) from the PNC source.

B. Laser fluence

The beam-area was indirectly determined by scanning the LGUS field from an epoxy-based PNC source using the hydrophone. A raster scan was undertaken over an area of 1.5 cm × 1.5 cm with 0.25 mm step size at an axial distance of 7.4 mm with the peak energy of the laser set to approximately 20 mJ. The beam-area of 0.8 cm^2 was estimated such that it included all pixels of the raster scan that were greater than or equal to 10% (or −20 dB) of the peak value in the image. This beam-area was then used to calculate the fluence, $mJ \cdot cm^{-2}$ at a number of peak energy settings of the laser, which was controlled by an inbuilt motorized waveplate. The beam-area was not dependent on laser energy. The raster scan of the LGUS field and the lateral profiles of the field in the *x*- and *y*- dimensions at the peak position of the raster scan is shown in Fig. 2.

The LGUS field shown in Fig. 2 is Gaussian, not planar. Consequently, the pressure will not be constant over the surface of the hydrophone, introducing a spatial averaging error in the measurement. However, the effect of hydrophone spatial averaging has been previously investigated in planar and nonlinearly steepened Gaussian shaped ultrasound fields. [9,51–53] At NPL a method developed by Zeqiri[51] is routinely applied, which requires the effective hydrophone diameter[24] and the −6 dB beam-width of the ultrasound field measured using the same hydrophone be known to calculate the magnitude of the spatial averaging error. For the UT1602 hydrophone, the −6 dB spectral beam-width averaged in the *x*- and *y*- dimensions up to 100 MHz was 6.5 mm with a standard deviation of 1.1 mm. Using a lower limit of 5.4 mm for the beam-width and assuming the geometrical diameter of 0.2 mm as the effective hydrophone diameter, the magnitude of the spatial averaging error was calculated to be less than 0.05%.

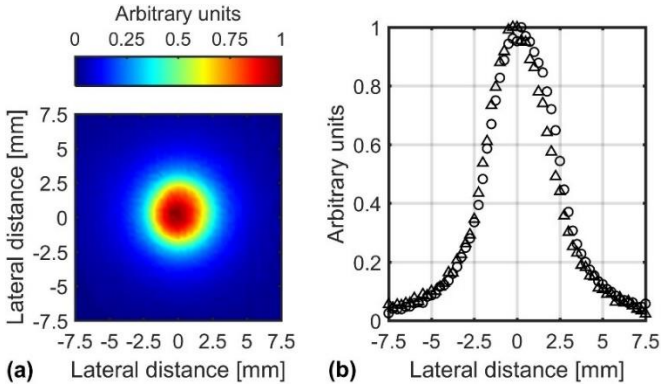

FIG. 2. (color online) (a) Raster scan of the LGUS field measured from an epoxy-based PNC source at an axial distance of 7.4 mm. The peak hydrophone voltages recorded from the raster scan shown in (a) is rescaled between (0, 1). (b) Lateral profiles of the LGUS field in *x*- and *y*-dimensions at the peak position of the raster scan are represented by circles and diamonds respectively.

C. Hydrophone response

The electrical response of the LGUS pulse acquired from the hydrophone at an axial distance z, $u(z,t)$ was converted to a pressure pulse, $p(z,t)$ via deconvolution[24] using the complex hydrophone sensitivity:

$$p(z,t) = \mathcal{F}^{-1}\left\{\frac{\mathcal{F}[u(z,t)]}{\underline{M}(f)}\right\}. \quad (2)$$

Here, $\mathcal{F}$ and $\mathcal{F}^{-1}$ are the Fourier and inverse Fourier transforms in time respectively, and $\underline{M}(f)$ is the complex frequency-dependent sensitivity response of the hydrophone. The UT1602 hydrophone was calibrated for its magnitude sensitivity and phase response between 1 and 60 MHz using a substitution method.[13,14] The frequency response of the hydrophone was also predicted from 1 to 110 MHz using a 1D analytical model previously developed at National Physical Laboratory.[54] An agreement between the measured and modelled response was obtained by optimizing the model input parameters (see Fig. 3). The measured phase response was obtained using a relative technique, which requires the magntiude sensitivity of the reference hydrophone to be flat implying the underlying phase response is a constant function of frequency.[12,14] Therefore, the technique used to measure the phase did not extend beyond 40 MHz. The gray uncertainty curves are plotted on the measured data, which are also extrapolated up to 110 MHz assuming a linear increase in uncertainty with frequency. The predicted response was used to deconvolve the hydrophone response from the measurements. The limit on the upper frequency of the predicted response was due to the unavailability of the impedance data for the hydrophone and preamplifier due to limited bandwidth of the impedance measuring device.

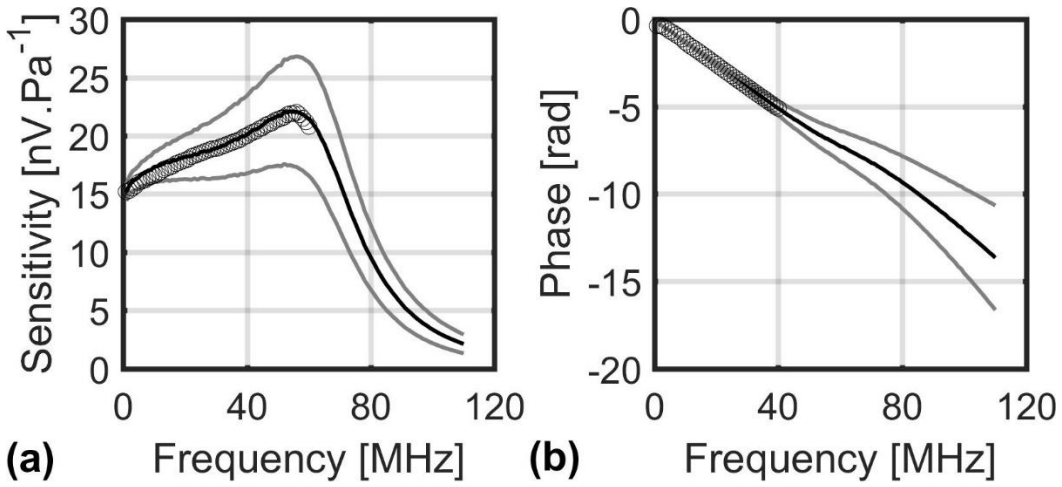

FIG. 3. Measured (circles) and predicted magnitude sensitivity and phase responses of UT1602 hydrophone are shown in (a) and (b) respectively. The gray uncertainty curves are plotted on the measured data, which are also extrapolated up to 110 MHz assuming a linear increase in uncertainty with frequency. The uncertainties are expressed at 95% coverage interval ($k = 2$). The uncertainties increase from 4.7% to 38% with frequency for the magnitude sensitivity and for phase it is 0.001 rad to 3.0 rad.

Since the sensitivity response of the hydrophone is not known beyond the extrapolated frequency range, for computational reasons the $\underline{M}(f)$ data up to the Nyquist frequency was assigned the same value as 110 MHz, and at 0 Hz the same value as determined for 1 MHz was assigned. After computing Eq. (2), the deconvolved pressure waveform was filtered using a Finite Impulse Response (FIR) linear-phase lowpass digital filter to remove frequency components beyond 110 MHz. The high frequency cut-off for the filter and the number of filter coefficients were set to 110 MHz and 24 respectively. This resulted in an attenuation of at least 26 dB of the magnitude components beyond twice the cut-off frequency.

The regularization of the deconvolution of hydrophone waveforms is currently an active field of study[4,10,14,55,56] but there is no standardized approach. A method to estimate the uncertainty bounds of the deconvolved hydrophone time-series waveform has been recently developed[57], which may

be useful when reporting of absolute exposure parameters from medical equipment is required for regulatory purposes. Since the primary aim of the present study is to assess the relative performance of 27 different PNC sources for their suitability as an ultrasound source for hydrophone calibrations, the regularization procedure described here was deemed sufficient.

IV. EXPERIMENTAL SOURCE CHARACTERISATION

A. Measured source pressures and bandwidths

The peak-positive pressure and the bandwidth (−6 dB) of the LGUS signal obtained from the 27 PNC sources were assessed as a function of polymer type, MWCNT wt% in each polymer, PNC thickness and laser fluence.[58] The effect of polymer type, MWCNT wt% and laser fluence are shown in Fig. 4. The relative performance of the PNC sources, under otherwise identical conditions, is largely governed by the polymer's coefficient of volume thermal expansion, β. According to the manufacturer's specification and from the literature, the coefficient of volume thermal expansion of cured epoxy, PU and PDMS are $75 \times 10^{-6}\,\mathrm{K}^{-1}$, $100 - 200 \times 10^{-6}\,\mathrm{K}^{-1}$ and $340 \times 10^{-6}\,\mathrm{K}^{-1}$, respectively.[59–61] For example, in Fig. 4(a) for 1.25 wt% MWCNT in the three polymers, and for a fluence of $10\ \mathrm{mJ \cdot cm^{-2}}$, the observed peak-positive pressures were 1.2, 1.6 and 2.0 MPa, respectively, which correlate with the β values of the pure polymers.

Increasing the weight content of MWCNT in PDMS (red circles in Fig. 4(a), Fig. 4(b) and Fig. 4(c)) from 1.25 to 2.5 wt% increased the peak-positive pressure from 6.2 to 6.7 MPa whereas at 3.5 wt%, the pressure increased only slightly more, to 6.8 MPa. Given the sound-speed of cured PDMS as $c_0 = 1050\ \mathrm{m \cdot s^{-1}}$, and using the optical absorption coefficients, μ_a in Table III, the acoustic relaxation time $(c_0\,\mu_a)^{-1}$ can be calculated for 1.25, 2.5 and 3.5 wt% CNT in PDMS to

be 14, 5.7 and 3.9 ns respectively. Since the duration of the laser pulse of 4 ns is approximately equal to the acoustic relaxation time for the case of 3.5 wt% MWCNT, the pressure confinement condition is not satisfied, i.e., the pressure wave starts to leave the heated region before the heating is completed, thereby limiting the magnitude of the acoustic pulse.[62–64]

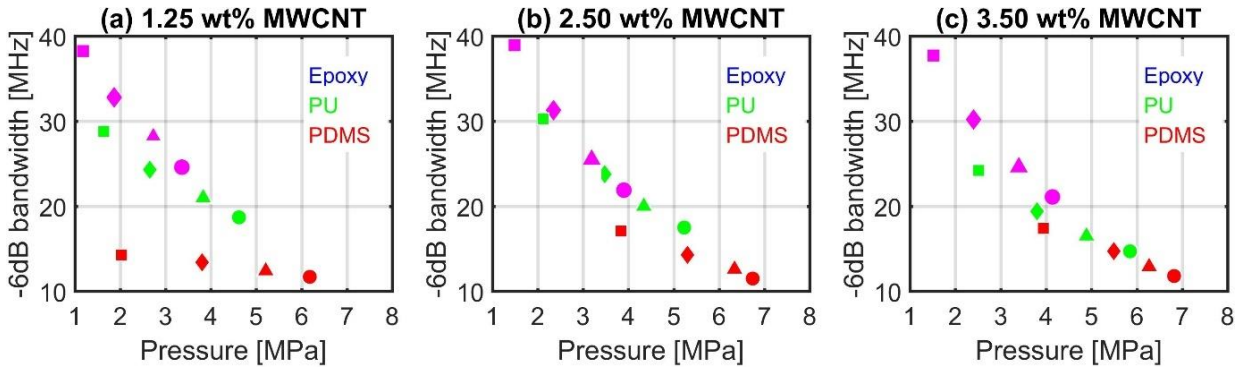

FIG. 4. (color online) Effect of polymer, MWCNT wt% and laser fluence are shown in (a), (b) and (c); The filled square, diamond, triangle and circle represent applied fluences of 10, 20, 30 and 40 $\mathrm{mJ \cdot cm^{-2}}$; PU—polyurethane; PDMS—polydimethylsiloxane; blue, green and red shapes represent epoxy, PU and PDMS. The results are representative of PNCs with an average thickness and standard deviation of 30 ± 4 µm.

Increasing the absorbed energy density, $\Phi\mu_a$, by increasing the laser fluence, Φ, according to Eq. (1), will increase the amplitude of the initial pressure distribution, $p_0(z)$, as shown in Fig 4. For example, the peak-positive pressures obtained for the case of epoxy PNC with 1.25 wt% for applied fluences of 10, 20, 30 and 40 $\mathrm{mJ \cdot cm^{-2}}$ are 1.2, 1.9, 2.7 and 3.4 MPa, respectively. This nonlinear increase in the peak-positive pressure as a function of applied fluence has been previously reported for PNC sources made of allotropes of carbon and also gold nanoparticle nanocomposites.[36,65,66] The reasons for this nonlinear increase have been attributed to the bandwidth limit of the hydrophone saturating its response,[65] partial detachment of the

nanocomposite film from the glass slide[36] and acoustic attenuation of LGUS pulse within the nanocomposite.[66]

In contrast, the nonlinear increase in pressure amplitude with fluence observed in this study is attributed to the nonlinear propagation coupled with acoustic absorption of the high amplitude LGUS pulse in water. It was also observed that the nonlinear increase in pressure amplitude (see Fig. 5) was accompanied by a decrease in −6 dB bandwidth (see Fig. 6). This is attributed to the broadening of the time-series pressure also as a consequence of the nonlinear propagation of LGUS pulse. It should be noted that the bandwidth (−6 dB) is a relative measure which describes the width of the emitted spectrum relative to the spectral peak, so a decrease in bandwidth does not necessarily imply that the higher frequency spectral magnitudes have decreased, as the overall amplitude may have increased. The effect of laser fluence on the pressure amplitude and −6 dB bandwidth due to nonlinear propagation is numerically investigated in Sec. V B. In Sec. V C, comparisons are shown between the model, convolved with the known hydrophone response, and the measured LGUS signals.

Finally, the thickness of the PNC source should be ideally equal to the optical absorption depth, $\mu_a{}^{-1}$: increasing the source thickness beyond $\mu_a{}^{-1}$ will not contribute towards pressure confinement but the additional PNC medium will attenuate the acoustic wave propagating through it. For a PU-based PNC with 1.25 wt% MWCNT, laser fluence of 20 mJ cm^{-2} and source thicknesses of 31, 51 and 78 μm, the calculated bandwidths from the LGUS pulses were 28, 21 and 18 MHz, respectively. The loss of bandwidth with increasing thickness is a clear demonstration of acoustic attenuation within the PNC material.

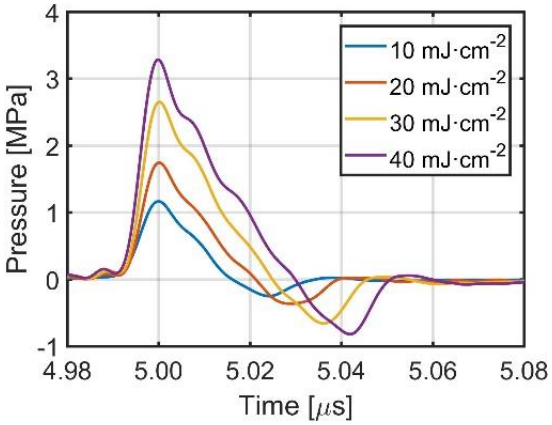

FIG. 5. (color online) Time-series pressure-pulses obtained for applied fluences of 10, 20 30 and 40 mJ · cm^{-2} from an epoxy PNC source dispersed with 1.25 weight-percent multiwalled carbon nanotubes and a nominal thickness of 27 µm.

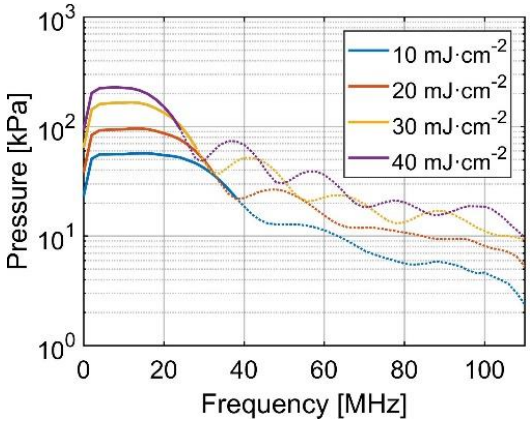

FIG. 6. (color online) Pressure spectra computed from the time-series pressure pulse to an applied fluence of 10, 20 30 and 40 mJ · cm^{-2} obtained from an epoxy PNC source dispersed with 1.25 weight-percent multiwalled carbon nanotubes and a nominal thickness of 27 µm. For each plot the −6 dB frequency span of 38, 33, 28 and 25 MHz to an applied fluence of 10, 20 30 and 40 mJ · cm^{-2} respectively is represented by a continuous curve followed by dotted curve of the same color.

B. Source stability

A preliminary study was undertaken on the stability of 17 PNC sources of which eight were epoxy, five were PU and four were PDMS-based polymers. All 17 PNC sources were loaded with 2.5 wt% MWCNT and were approximately 10 μm in thickness. The stability of the PNC source under test was assessed by analyzing the peak-positive voltages of the hydrophone measurements. PNC sources were tested at two fluence levels of 20 and 30 $\mathrm{mJ \cdot cm^{-2}}$ for one hour at a pulse repetition rate of 20 Hz. During testing, the majority of the epoxy and PU-based PNC sources suffered visible damage i.e., the PNC film detached from the surface of the glass slide. The adhesion of the PNC to the glass surface is affected by the surface chemistry, so precautions were taken during fabrication to clean the surface of the glass to remove dirt and grease using acetone and methanol. However, both cured epoxy and PU are hydrophilic due to the presence of electronegative functional groups such as hydroxyl and ester groups. Therefore, water take-up and/or ingression may have weakened the adhesion of the PNC film to glass.

A common trend was observed in all PNC sources in which the LGUS amplitude gradually decreased over the duration of the measurement (see Fig. 7). The observed trend correlates with the change in temperature of the PNC medium, which was determined by measuring the surface temperature of the PNC in contact with water approximately near the area of maximum laser fluence. The surface temperature of the PNC increased by 8.5 ℃ for a laser fluence of 30 $\mathrm{mJ \cdot cm^{-2}}$, and became stable in approximately 10 minutes. The temperature increase thereafter was only 0.2 ℃ over a 50-minute measurement period. Since the Grüneisen parameter is temperature dependent, the LGUS amplitude is directly affected by the temperature. Once a temperature equilibrium was reached the change in LGUS output was minimal i.e., it gradually decreased by

1% over the rest of the measurement period. Although efforts will be made to improve on this performance, it is already considered adequate with regard to allowing the calibration of hydrophones with acceptable uncertainties. The calibration of a hydrophone on the primary standard involves obtaining a pair of measurements i.e., a hydrophone voltage signal and the interferometer signal corresponding to either acoustic displacement or particle velocity, which are acquired consecutively. These measurements are normally completed within 20 mins and at least six pairs of independent measurements are taken to obtain confidence in the calibration data. If the LGUS output gradually decreases, then a gradual change in sensitivity can be expected over the duration of the calibration. The slope of the characteristic trend can then be used to apply an approximate correction to remove the gradual change in the sensitivity provided the random uncertainty in the calibration data is better than 1%.

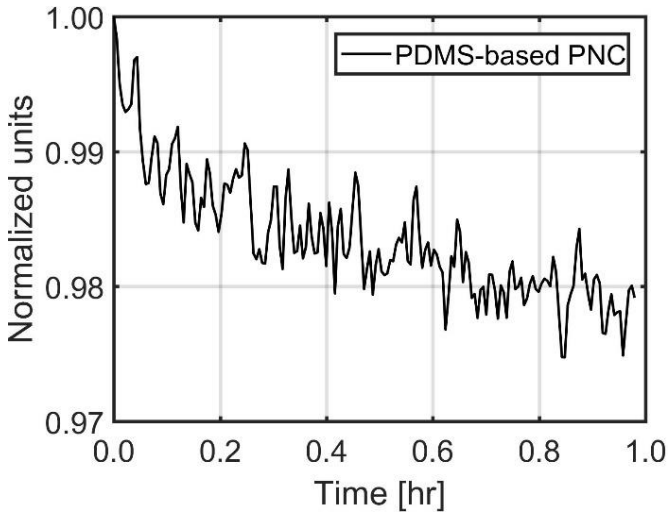

FIG. 7. Stability curve of a PDMS-based PNC source when tested over one-hour period at a laser fluence of 30 $\mathrm{mJ \cdot cm^{-2}}$. The polymer was loaded with 2.5 wt% MWCNT and the PNC is approximately 10 µm thick. The plotted curve was computed by normalizing the peak-positive voltages of the hydrophone measurements, which were not corrected for laser fluence variations. The decrease in normalized output from the PNC over time does not correlate with laser fluence variations. The variation in the laser output was found to be random with better than 2% variation after a warm-up period of 30 mins.

The PNC film detachment from the glass surface in the case of epoxy and PU-based PNCs is currently hypothesized to be due to its weak adhesion to the glass surface caused by hydrophilic nature of the polymer matrices. For a thicker PNC film, the water take-up and/or ingression may be slower, affecting the adhesion differently, which remains to be tested. But increasing the PNC thickness affects the bandwidth of the LGUS pulse due to increased ultrasound absorption with frequency compared to water. Therefore, epoxy or PU is not a preferred polymer matrix for the present application. Although, only four PDMS PNC sources were tested for stability, the results favor PDMS over epoxy and PU-based PNC sources. However, more PDMS PNC sources will be tested in a subsequent study to gain further understanding of the source behavior under extended laser pulse excitation.

V. NUMERICAL SIMULATIONS

A. Acoustic propagation model

In Sec. IV it was hypothesized that the broadening of the time-series pressure pulse and the consequent reduction in bandwidth (−6 dB) as the amplitude was increased was caused by the cumulative acoustic nonlinearity due to propagation of high amplitude LGUS in water over a measurement distance of 7.4 mm. This leads to steepening of the LGUS wavefront i.e., the steep edge of the initial pressure distribution physically transforms from back to front as the wave propagates, with steepening becoming prominent with increasing amplitude of the LGUS pulse. This change in wave shape transformation broadens the pulse. To demonstrate this, 1D numerical simulations were performed using k-Wave, a third party open-source toolbox for MATLAB (MathWorks, Inc., Natick, Massachusetts), which can model nonlinear acoustic propagation in

media obeying power law absorption.[67–69] k-Wave solves a generalized form of the Westervelt equation valid for heterogeneous media with power law absorption

$$\nabla^2 p - \frac{1}{c_0^2}\frac{\partial^2 p}{\partial \mathrm{t}^2} - \frac{1}{\rho_0}\nabla\rho_0 \cdot \nabla p + \left(1 + \frac{B}{2A}\right)\frac{1}{\rho_0 c_0^4}\frac{\partial^2 p^2}{\partial t^2} - L\nabla^2 p = 0, \tag{3}$$

where the term $(1 + B/2A)$ is the coefficient of nonlinearity and B/A is the nonlinearity parameter, ρ_0 is the ambient density in units of $\mathrm{kg \cdot m^{-3}}$ and L is the loss operator.[69] For all simulations, convergence tests were carried out by reducing the size of grid spacing and time-step to ensure that the solution was accurate and numerical artefacts did not corrupt the time-series.[70]

B. Effect of nonlinear propagation

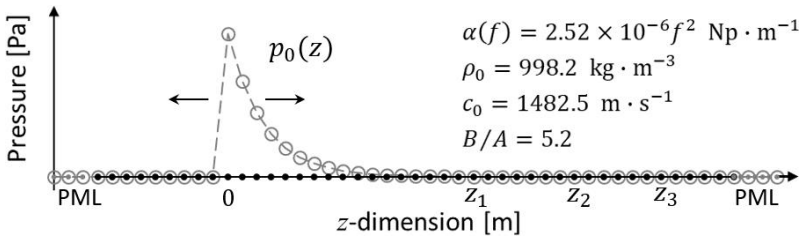

FIG. 8. Schematic of the 1D computational grid implemented in k-Wave to investigate the broadening of time-series pressure-pulse due to nonlinear propagation of high amplitude laser generated ultrasound pulse in water as function of laser fluence. PML—perfectly matched layer, $p_0(z)$—initial pressure distribution defined using Eq. (1), B/A—nonlinear parameter of water, c_0—sound-speed of water, ρ_0—ambient density of water, f—frequency in MHz, $\alpha(f)$—frequency dependent acoustic absorption of water, z_1, z_2 and z_3—specified grid points for recording time-series pressure-pulse, $p(z,t)$. The grid is not to scale.

The schematic of the 1D numerical grid to investigate the effect of nonlinear propagation is shown in Fig. 8. The PNC medium was modelled as water. However, this will have little effect on the results since the thickness of PNC source is small (the thickest PNC source was 70 μm) compared to the propagation distance of 7.4 mm. The spatial profile of the initial pressure distribution $p_0(z)$

was computed using Eq. (1) assuming β = 72.5 × 10^{-6} K^{-1}, C_p = 1110 J Kg^{-1} K^{-1}, c_0 = 2600 m · s^{-1},[59,71,72] which correspond to values for the cured epoxy polymer family, and μ_a = 125,000 m^{-1}, which corresponds to the optical absorption coefficient of epoxy PNC with 2.5 wt% MWCNT. The laser fluence, Φ was varied such that the peak-positive initial pressure varied in the range 5.5 to 22 MPa in steps of 1.4 MPa, giving peak-positive pressures of $p(z,t)$ in the range 2.75 to 11 MPa. These amplitudes were chosen such that the recorded amplitudes of the time-series, $p(z,t)$ at 7.4 mm were within the range of experimentally measured values of 1.2 to 6.9 MPa (see Fig. 4). The time-series pressure-pulse, $p(z,t)$, was recorded at 0.2 mm increments from $p_0(z)$ so that the time-series could be analyzed for the effects of nonlinear propagation.

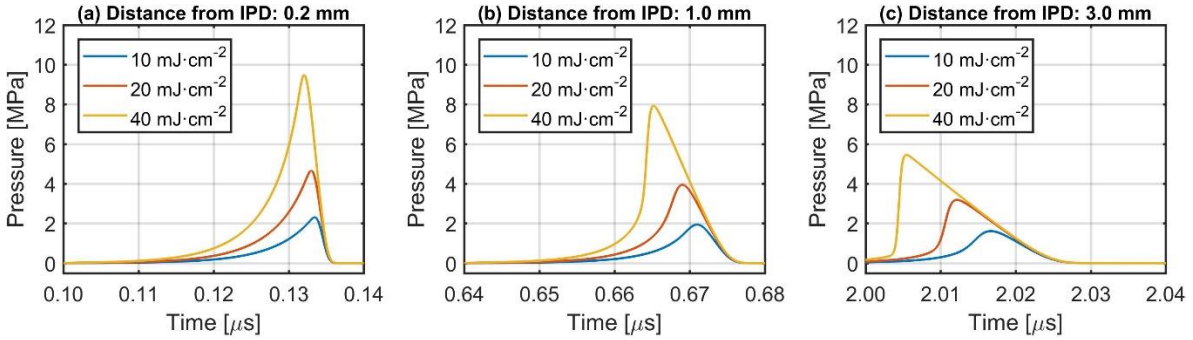

FIG. 9. (color online) Steepening of the time-series pressure-pulse caused by cumulative acoustic nonlinearity as a function of pressure amplitude and propagation distance for laser fluence of 10, 20 and 40 mJ · cm^{-2} are shown in (a), (b) and (c). The steepening of the pressure-pulse is accompanied with broadening of the time-series, which is prominent for the case of 40 mJ · cm^{-2} and a propagation distance of 3.0 mm is seen in (c). The optical absorption depth for this simulation was set to 50 µm to emphasize the effect of wave shape transformation due to cumulative acoustic nonlinearity.

The time-series pressure pulses shown in Fig. 9 correspond to simulation results for an optical absorption depth of 50 µm, which was chosen to emphasize the effect of wave shape transformation due to cumulative acoustic nonlinearity. The time-series recorded at 0.2 mm from $p_0(z)$ have clear exponential profiles (see Fig. 9(a)) for all three laser fluences of 10, 20 and

40 mJ cm^{-2}. But as the wave propagates further away from $p_0(z)$, the cumulative acoustic nonlinearity increase transforming the steep edge of $p(z,t)$ in the direction of propagation. The degree to which the wave shape transforms to a steepened wave is dependent on both the propagation distance and the amplitude of $p_0(z)$. This progressive change can be seen in Fig. 9(a) through to Fig. 9(c). These simulations suggest that the LGUS pulses seen in measurements for example Fig. 5 are affected by nonlinear propagation. This is confirmed with comparisons to measured time-series in Sec. V C below. The supplementary material provides animations of the wave shape transformation shown in Fig. 9.[76]

The effect of acoustic absorption and time-series broadening due to nonlinear propagation on the pressure amplitude and bandwidth (−6 dB) are shown in Fig. 10 and Fig. 11 respectively. The peak-positive pressures of the simulated time-series pressure pulses and the bandwidths obtained from their magntitude spectra are plotted in Fig. 10(a) and Fig. 11(a) as a function of source-sensor separation and laser fluence. For improved comparison truncated simulation data is plotted in Fig. 10(b) and Fig. 11(b), which overlaps with the source-sensor separation of the measured data. The simulations correspond to an optical absorption depth of 10 μm. The measured results from an epoxy PNC of 10 μm thickness with 2.5 wt% MWCNT are shown in Fig. 10(c) and Fig. 11(c) over the same fluence range but the closest source-hydrophone distance was 3.9 mm as opposed to 0.2 mm in the simulations. This is because the hydrophone signal chain was susceptible to radio-frequency noise emitted by the Q-switch of the laser, which lasted for up to 2.5 μs and hence the hydrophone could not be positioned closer than 3.9 mm (or 2.63 μs in time-of-flight). The pressures shown in Fig. 10(b) and Fig. 10(c) agree to within 50 kPa (or 1%). This was achieved by scaling the Grüneisen parameter, Γ used to compute the $p_0(z)$ by 1.25. However, the

bandwidths shown in Fig. 11(b) and Fig. 11(c) differ by 5 MHz. This is attributed to the differences in the physical make up of the PNC source in simulation and measurement. For the case of epoxy PNC upon excitation by a pulsed laser, the backward propating pressure pulse reflected at the glass-epoxy PNC interface immediately follows the forward propagating wave increasing the duration of the LGUS pulse. However, for simulations a homogenous medium was assumed, therefore the duration of the forward propagating pressure pulse is unaffected by the backward propagating pressure pulse. These results also suggest that an inverse relationship exists between the amplitude of the time-series pressure pulse and its bandwidth. The decrease in bandwidth means that the pressure amplitudes at higher frequencies are relatively lower, which means that the signal-to-noise will be lower. Therefore, the measured displacement or velocity from the interferometers will be lower increasing both the random and systematic uncertainty of the measurement. As a consequence of this, in order to improve the quality of the calibration of hydrophones at high frequencies, the hydrophone should be positioned as close as practically achievable to the PNC source.

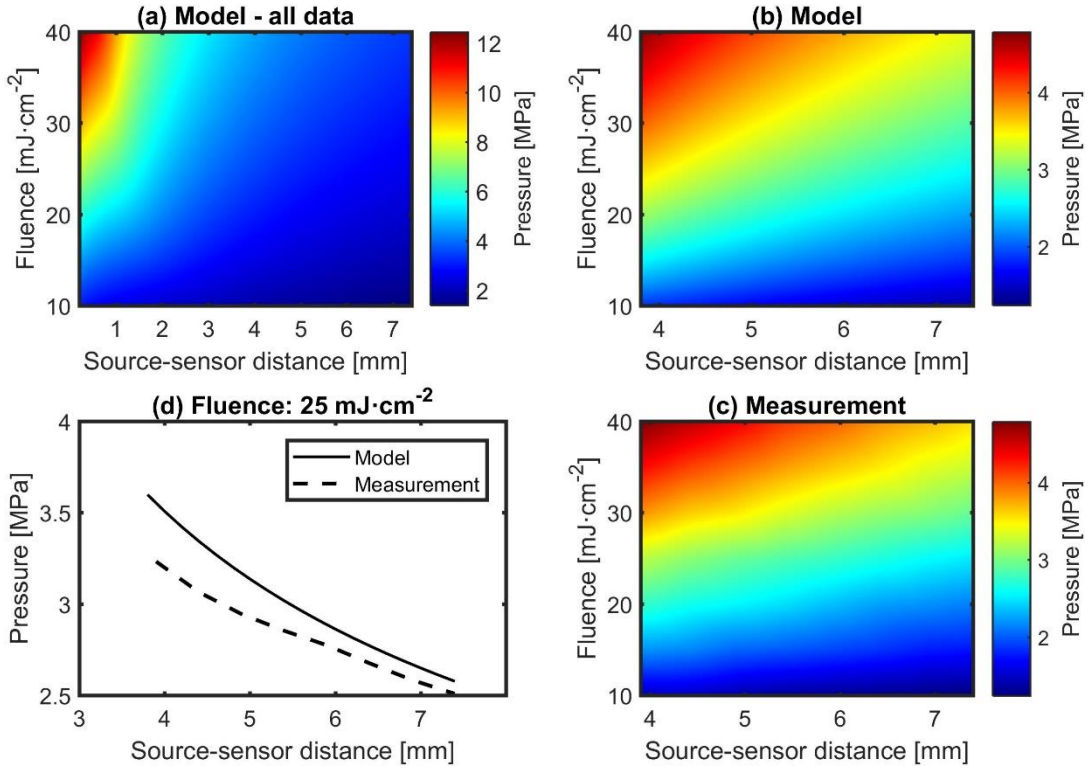

FIG. 10. (color online) (a) Peak-positive pressures of the simulated time-series pressure pulses using k-Wave as a function of fluence and source-sensor separation. The optical absorption depth was set to 10 μm. Truncated simulation data is shown in (b) for improved comparison with measured data in (c), which overlaps with the source-sensor separation of the measured data. (c) Measured peak-positive pressures from an epoxy polymer nanocomposite source dispersed with 2.5 wt% MWCNT and a thickness of approximately 10 μm. The hydrophone could not be positioned below 3.9 mm (or 2.63 μs in time-of-flight) due to pick up of radio-frequency noise emitted by the Q-switch of the laser, which lasted for up to 2.5 μs. (d) Line plot of model and measured pressures at 25 $\mathrm{mJ \cdot cm^{-2}}$.

1

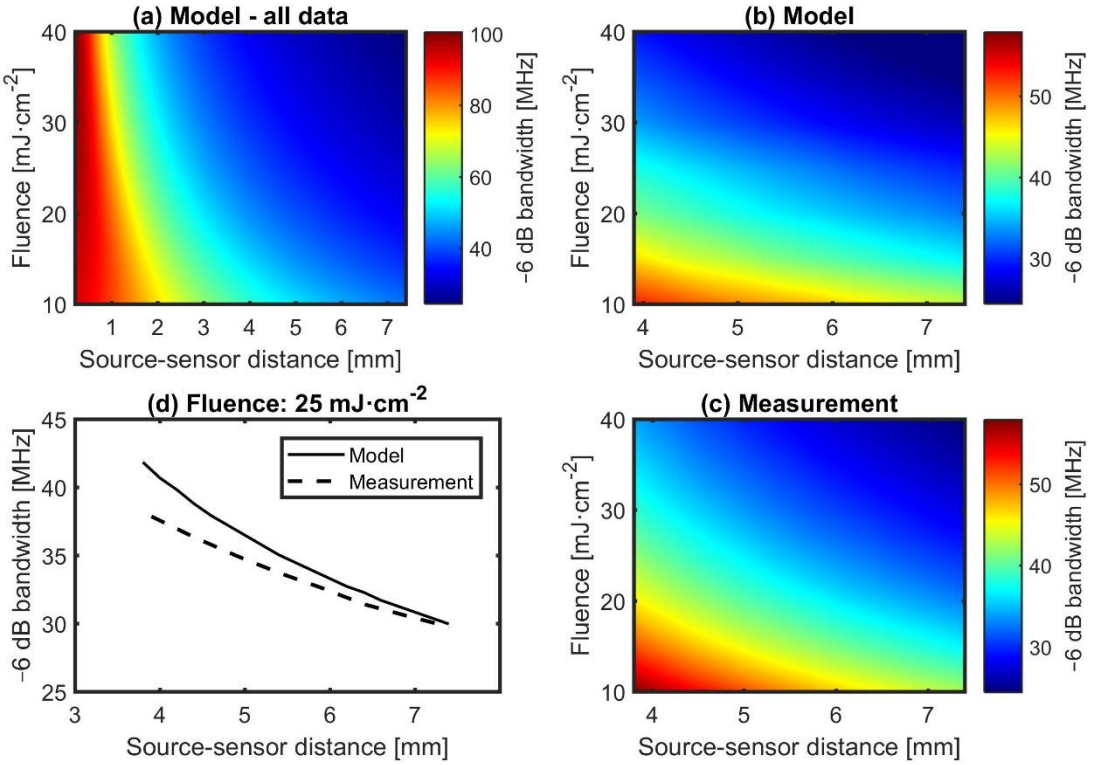

FIG. 11. (color online) (a) −6 dB bandwidths of the simulated time-series pressure pulses using k-Wave as a function of fluence and source-sensor separation. The optical absorption depth was set to 10 µm. Truncated simulation data is shown in (b) for improved comparison with measured data in (c), which overlaps with the source-sensor separation of the measured data. (c) Measured bandwidths (−6 dB) from an epoxy polymer nanocomposite source dispersed with 2.5 wt% MWCNT and a thickness of approximately 10 µm. The hydrophone could not be positioned below 3.9 mm (or 2.63 µs in time-of-flight) due to pick up of radio-frequency noise emitted by the Q-switch of the laser, which lasted for up to 2.5 µs. (d) Line plot of model and measured bandwidths at 25 mJ · cm^{-2}.

C. Effect of bandlimited hydrophone response

Comparing the simulation pulses in Fig. 9 with the measured pulses in Fig. 5, there are clear qualitative differences. Since these LGUS pulses have a wider bandwidth than the hydrophone, it was hypothesized that the bandlimited response of the hydrophone was a likely cause for the difference between the simulation and the measurements. To test this, pressure time-series were simulated for an epoxy PNC source of 10 µm thickness sandwiched between glass and water half spaces. The output of the acoustic model was convolved with the sensitivity response of the

hydrophone from 1 to 110 MHz used in the deconvolution procedure in Sec. III C. The time-series pressure pulse, $p(z,t)$, recorded at a grid location of 7.4 mm in water medium from $p_0(z)$ was then convolved with complex sensitivity response of the hydrophone to derive the model voltage, $u_{model}(z,t)$ as follows:

$$u_{model}(z,t) = \mathcal{F}^{-1}\{\mathcal{F}[p_{model}(z,t)] \times \underline{M}(f)\}. \quad (4)$$

Here, $p_{model}(z,t)$ is the simulated pressure pulse. Since the time-steps in the simulation and measurement were different i.e., 4.4326 ps and 400 ps respectively, the simulated $p_{model}(z,t)$ was down-sampled using MATLAB's *resample* function to match with the sampling frequency of the measured oscilloscope. $\underline{M}(f)$ was set to zero at 0 Hz and beyond 110 MHz (see Fig. 3). The resulting voltage time-series, $u_{model}(z,t)$, was then compared with the measured hydrophone voltage time-series, $u_{meas}(z,t)$, obtained from a 10 μm thick epoxy PNC with 2.5 wt% MWCNT. The amplitude of $p_0(z)$ was varied by scaling the Grüneisen parameter, Γ such that the amplitude of $p_{model}(z,t)$ at 7.4 mm was approximately equal to the deconvolved pressure pulse for applied fluence levels of 10, 20 and 40 $\text{mJ} \cdot \text{cm}^{-2}$ in the experiment. The scaled values of Γ at the four fluence levels were 1.85, 1.95 and 2.12.

The time-series agreement shown in Fig. 12 was obtained by adjusting the mass density and sound-speed of epoxy PNC. The mass density value is within the expected range[73] however, there are no literature values available for sound-speed. The acoustic attenuation of glass is irrelevant since only the forward propagating wave from within the PNC medium into the water medium is of interest. The acoustic loss within k-Wave is implemented as a power-law model: $\alpha = \alpha_0\, \omega^y$ using

a fractional Laplacian operator[69], where α is the absorption coefficient in units of $\mathrm{Np} \cdot \mathrm{m}^{-1}$, α_0 is the power law prefactor in $\mathrm{Np}\ (\mathrm{rad/s})^{-y} \cdot \mathrm{m}^{-1}$, y is the power law exponent and ω is the angular frequency. This approach allows heterogeneous media to have different power law absorption prefactors, but the power law exponent must be the same for all media. Therefore, considering these limitations, the acoustic absorption for glass and epoxy PNC were assumed to be that of water.

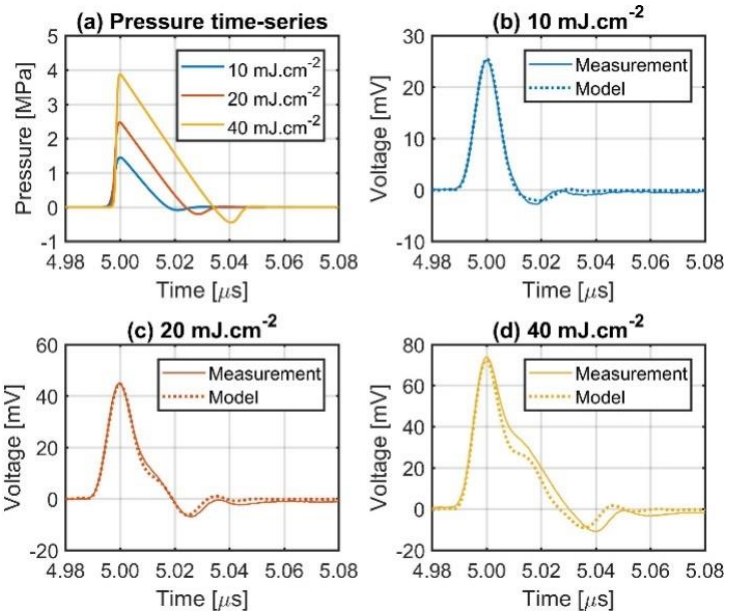

FIG. 12. (color online) (a) Pressure time-series simulated using k-Wave in 1D from a three layered media comprising of 10 μm thick epoxy PNC with 2.5 wt% multiwalled carbon nanotubes sandwiched between glass and water half spaces. The time-series was recorded at a distance of 7.4 mm from the initial pressure distribution for laser fluences of 10, 20 and 40 $\mathrm{mJ} \cdot \mathrm{cm}^{-2}$. Model derived voltage time-series obtained by convolving the pressure time-series in (a) with the complex sensitivity response of the hydrophone (see Fig. 3) are plotted along with the measured voltage time-series for laser applied fluences of (b) 10, (c) 20 and (d) 40 $\mathrm{mJ} \cdot \mathrm{cm}^{-2}$. The two time-series were aligned by shifting the model derived voltage time-series with respect to measured time-series.

Table IV. Model input parameters used in 1D k-Wave for the generation of time-series pressure pulses from an epoxy polymer nanocomposite backed on glass and radiating acoustic wave in water media. The values for the mass density and sound-speed of epoxy PNC were varied approximately by 10 and 25% respectively to achieve a closest agreement of model derived voltage time-series with the measurements. The optical absorption coefficient was measured, and remaining values were obtained from references: [59,71,74,75].

Parameter	Material	Value	Units
Mass density, ρ_0	Pyrex glass Epoxy Water	2230 749 998.2	$kg \cdot m^{-3}$
Sound speed, c_0	Pyrex glass Epoxy Water	5640 2300 1482.5	$m \cdot s^{-1}$
Acoustic absorption, $\alpha(f)$	Water	$2.52 \times 10^{-6} f^2$	$Np \cdot m^{-1}$
Optical absorption coefficient, μ_a	Epoxy-PNC	125000	m^{-1}
Coefficient of thermal expansion, β	Epoxy	72.5×10^{-6}	m^{-1}
Specific heat capacity, C_p	Epoxy	1110	$J \cdot kg^{-1} \cdot K^{-1}$

There is a good agreement between measured and model derived voltage time-series for the case of 10 and 20 mJ cm^{-2} shown in Fig. 12(b) and Fig. 12(c) respectively, which confirms that the predicted sensitivity response is approximately close to the true sensitivity response of the hydrophone and its limited bandwidth is the dominant cause for the presence of undulations in the deconvolved time-series pressure pulses (see Fig. 5). However, in Fig. 12(d) at 40 $mJ \cdot cm^{-2}$, the trailing part of the model-derived voltage time-series is slightly offset from the measured voltage time-series. It suspected that this difference could be due to a change in the behavior of the Grüneisen parameter of epoxy PNC as the fluence increases beyond 20 $mJ \cdot cm^{-2}$. Assuming thermal confinement, the initial temperature rise is given by $T_0 = \mu_a \Phi / \rho_0 C_p$. For a fluence, Φ =

400 J m^{-2} (or 40 mJ $\cdot$ cm^{-2}), optical absorption coefficient, μ_a = 125000 m^{-1}, which corresponds to 2.5 wt% MWCNT in epoxy and assuming mass density, ρ_0 and specific heat capacity, C_p to be 1070 kg m^{-3} and 1110 J $\cdot$ kg^{-1} $\cdot$ K^{-1}, respectively then the initial temperature rise works out to be 42 ℃ above ambient temperature. Therefore, the material properties cannot be assumed to vary linearly during the heating phase of the PNC medium, consequently affecting the shape of the initial pressure distribution, $p_0(z)$.

Although PDMS-based PNC sources are favored over epoxy and PU-based PNC sources given its stability, the simulations and its comparison to measurements were all based on epoxy-based PNC sources. This is because the pulse broadening due to cumulative acoustic nonlinearity is more clearly discernible in these simulations. The reason is that the pressure output from PDMS-based PNC was approximately a factor of two higher than epoxy or PU-based PNC, so the pulses had broadened by the time they reached the measurement location whatever the fluence level. For epoxy, as the pressures were lower, the effect of the different fluence levels can be seen more clearly (see supplementary video, in which pulse broadening occurs over a shorter distance for the case of 40 mJ $\cdot$ cm^{-2} compared to 10 mJ $\cdot$ cm^{-2}). Simulations were also undertaken for PDMS-based PNC to investigate the effect of bandlimited hydrophone response and the quality of its agreement with measurements were found to be comparable to those reported in Fig. 12. Nevertheless, these results support the conclusion that the broadening of the time-series pressure pulse and the consequent reduction in bandwidth (−6 dB) as the amplitude increased was caused by the cumulative acoustic nonlinearity due to propagation of high amplitude LGUS in water.

VI. CONCLUSION

LGUS pulses from PNC sources made of bulk polymer matrix dispersed with MWCNT on a laboratory-grade glass slide were examined as a function of polymer type, MWCNT weight content in the polymer, PNC thickness and laser fluence. The study found that:

- for nominally identical PNCs and a given laser fluence, the amplitude of the LGUS was found to be directly proportional to volume thermal expansion coefficient of the polymer.
- for a given duration of the laser pulse, increasing the MWCNT content did not increase the LGUS response since the acoustic transit time across the optical absorption depth is shorter than the laser pulse duration, limiting the stress confinement due to medium relaxation. Similarly, the PNC source thickness should ideally be equal to the optical absorption depth to minimize acoustic attenuation and loss of bandwidth.
- the peak pressure from the PNCs was found to be nonlinearly dependent on the laser fluence and the bandwidth scaled inversely proportionally to the peak pressure. This was caused by the steepening of the LGUS wavefront i.e., the steep edge of the initial pressure distribution physically transforms from back to front as the wave propagates, with steepening becoming prominent as the amplitude of the LGUS pulse increased with applied fluence.
- the changing wave shape coupled with rapid absorption of high frequencies in water relative to lower frequencies resulted in loss of both amplitude and bandwidth as confirmed with measurements and modelling studies.
- a preliminary study of the stability of the PNCs under sustained laser illumination revealed that epoxy and PU PNCs were unstable due their hydrophilic nature whilst PDMS PNC was found to be most stable due its hydrophobic nature. A steady decrease in LGUS output was observed

from all stable PNC sources. The rate of decrease was generally 1% or less after the first 10 mins. Simple assumptions suggest that this steady decrease would have a negligible consequence on hydrophone calibration.

Overall, the nanocomposite materials studied show promise as the basis of standard sources supporting the high frequency calibration of hydrophones. Further studies will be targeted at developing a physical understanding of the reasons for the small fall-off in stability of the LGUS signal generated and an assessment of its impact on hydrophone calibrations.

ACKNOWLEDGMENT

The UK Department for Business, Energy & Industrial Strategy's funding of the National Measurement System is gratefully acknowledged. SR thanks National Physical Laboratory (NPL) for supporting his PhD at University College London, and the Composites, Adhesives and Polymeric Materials Group at NPL for providing access to laboratory facilities to undertake the nanocomposite work. BC and BT acknowledge the European Union's Horizon 2020 research and innovation program H2020 ICT 2016-2017 under grant agreement No 732411, which is an initiative of the Photonics Public Private Partnership.

REFERENCES

[1] 62127-1:2007+AMD1:2013: Amendment 1 - Ultrasonics - Hydrophones - Part 1: Measurement and characterization of medical ultrasonic fields up to 40 MHz, International Electrotechnical Commission, Geneva, 2013.

[2] IEC 60601-2-37:2007 Medical electrical equipment - Part 2-37: Particular requirements for the basic safety and essential performance of ultrasonic medical diagnostic and monitoring equipment, International Electrotechnical Commission, Geneva, 2015.

[3] IEC 60601-2-62:2013 Medical electrical equipment - Part 2-62: Particular requirements for the basic safety and essential performance of high intensity therapeutic ultrasound (HITU) equipment, International Electrotechnical Commission, Geneva, 2013.

[4] V. Wilkens, S. Sonntag, O. Georg, Robust spot-poled membrane hydrophones for measurement of large amplitude pressure waveforms generated by high intensity therapeutic ultrasonic transducers, J. Acoust. Soc. Am. 139 (2016) 1319–1332. doi:10.1121/1.4944693.

[5] P. Morris, A. Hurrell, E. Zhang, S. Rajagopal, P. Beard, A fabry-perot fibre-optic hydrophone for the measurement of ultrasound induced temperature changes, in: Proc. - IEEE Ultrason. Symp., 2006. doi:10.1109/ULTSYM.2006.139.

[6] S.M. Howard, Calibration of reflectance-based fiber-optic hydrophones, IEEE Int. Ultrason. Symp. IUS. 2016–Novem (2016) 2–5. doi:10.1109/ULTSYM.2016.7728572.

[7] E. Martin, E.Z. Zhang, J.A. Guggenheim, P.C. Beard, B.E. Treeby, Rapid Spatial Mapping of Focused Ultrasound Fields Using a Planar Fabry-Pérot Sensor, IEEE Trans. Ultrason. Ferroelectr. Freq. Control. 64 (2017) 1711–1722. doi:10.1109/TUFFC.2017.2748886.

[8] A. Hurrell, Voltage to pressure conversion: are you getting `phased' by the problem?, J. Phys. Conf. Ser. 1 (2004) 57–62. doi:10.1088/1742-6596/1/1/014.

[9] V. Wilkens, C. Koch, Amplitude and phase calibration of hydrophones up to 70 MHz using broadband pulse excitation and an optical reference hydrophone, J. Acoust. Soc. Am. 115 (2004) 2892–2903. doi:10.1121/1.1707087.

[10] K.A. Wear, P.M. Gammell, S. Maruvada, Y. Liu, G.R. Harris, Improved measurement of acoustic output using complex deconvolution of hydrophone sensitivity, IEEE Trans. Ultrason. Ferroelectr. Freq. Control. 61 (2014) 62–75. doi:10.1109/TUFFC.2014.6689776.

[11] M. Weber, V. Wilkens, Using a heterodyne vibrometer in combination with pulse excitation for primary calibration of ultrasonic hydrophones in amplitude and phase, Metrologia. 54 (2017) 432–444. doi:10.1088/1681-7575/aa72ba.

[12] C. Koch, Amplitude and phase calibration of hydrophones by heterodyne and time-gated time-delay spectrometry, IEEE Trans. Ultrason. Ferroelectr. Freq. Control. 50 (2003) 344–348. doi:10.1109/TUFFC.2003.1193629.

[13] R.A. Smith, D.R. Bacon, A multiple-frequency hydrophone calibration technique., J. Acoust. Soc. Am. 87 (1990) 2231–2243. doi:10.1121/1.399191.

[14] A.M. Hurrell, S. Rajagopal, The practicalities of obtaining and using hydrophone calibration data to derive pressure waveforms, IEEE Trans. Ultrason. Ferroelectr. Freq. Control. 64 (2016) 126–140. doi:10.1109/TUFFC.2016.2594770.

[15] "MicroScan™ Transducers.," FUJIFILM Vis. (2016). http://www.visualsonics.com/products/vevo-2100/ms-transducers (accessed October 17, 2016).

[16] ArcScan Insight® 100 Scanner, ArcScan Inc. (2016).

https://www.arcscan.com/solutions/arcscan-insight-system/arcscan-insight-100-scanner/ (accessed October 17, 2016).

[17] DermaScan C USB Ultrasound Series, CORTEX Technol. ApS. (2016). http://www.cortex.dk/skin-analysis-products/dermascan-ultrasound.aspx (accessed October 17, 2016).

[18] J.E. Kennedy, G.R. Ter Haar, D. Cranston, High intensity focused ultrasound: surgery of the future?, Br. J. Radiol. 76 (2003) 590–599. doi:10.1259/bjr/17150274.

[19] D.L. Miller, N.B. Smith, M.R. Bailey, G.J. Czarnota, K. Hynynen, I.R.S. Makin, Bioeffects Committee of the American Institute of Ultrasound in Medicine, Overview of therapeutic ultrasound applications and safety considerations., J. Ultrasound Med. 31 (2012) 623–34. doi:10.1016/j.biotechadv.2011.08.021.Secreted.

[20] D.R. Bacon, Primary Calibration of Ultrasonic Hydrophone Using Optical Interferometry., IEEE Trans. Ultrason. Ferroelectr. Freq. Control. 35 (1988) 152–161. doi:10.1109/58.4165.

[21] C. Koch, W. Molkenstruck, Primary calibration of hydrophones with extended frequency range 1 to 70 MHZ using optical interferometry, IEEE Trans. Ultrason. Ferroelectr. Freq. Control. 46 (1999) 1303–1314. doi:10.1109/58.796135.

[22] Y. Matsuda, M. Yoshioka, T. Uchida, T. Kikuchi, Absolute calibration of membrane hydrophones up to 40 MHz in ultrasonic far-field, IEEE Int. Ultrason. Symp. IUS. (2012) 374–377. doi:10.1109/ULTSYM.2012.0092.

[23] P. Yang, G. Xing, L. He, Calibration of high-frequency hydrophone up to 40 MHz by heterodyne interferometer, Ultrasonics. 54 (2014) 402–407. doi:10.1016/j.ultras.2013.07.013.

[24] 62127-2:2007+AMD1:2013: Amendment 1 - Ultrasonics - Hydrophones - Part 2: Calibration for ultrasonic fields up to 40 MHz, International Electrotechnical Commission, Geneva, 2013.

[25] V. Wilkens, W. Molkenstruck, Broadband PVDF Membrane Hydrophone for Comparisons of Hydrophone Calibration Methods up to 140 MHz, IEEE Trans. Ultrason. Ferroelectr. Freq. Control. 54 (2007) 1784–1791. doi:10.1109/TUFFC.2007.462.

[26] R.M. White, Generation of Elastic Waves by Transient Surface Heating, J. Appl. Phys. 34 (1963) 3559. doi:10.1063/1.1729258.

[27] M.W. Sigrist, Laser generation of acoustic waves in liquids and gases, J. Appl. Phys. 60 (1986) R83. http://scitation.aip.org/content/aip/journal/jap/60/7/10.1063/1.337089 (accessed December 22, 2014).

[28] A.C. Tam, Appliacations of photoacoustic sensing techniques, Rev. Mod. Phys. 58 (1986) 381–431. doi:10.1103/RevModPhys.58.381.

[29] S.-L. Chen, Review of Laser-Generated Ultrasound Transmitters and Their Applications to All-Optical Ultrasound Transducers and Imaging, Appl. Sci. 7 (2016) 25. doi:10.3390/app7010025.

[30] X. Fan, Y. Baek, K. Ha, M. Kim, J. Kim, D. Kim, H.W. Kang, J. Oh, Propagation characteristics of shock waves from a plane carbon-nanotube-coated optoacoustic transducer in water, Jpn. J. Appl. Phys. 56 (2017) 5–8. doi:10.7567/JJAP.56.07JB05.

[31] C. Moon, X. Fan, K. Ha, D. Kim, Generation of planar blast waves using carbon nanotubes-poly-dimethylsiloxane optoacoustic transducer, AIP Adv. 7 (2017) 015107. doi:10.1063/1.4974748.

[32] H.W. Baac, T. Ling, H.J. Park, L.J. Guo, Evaluation of Optoacoustic Conversion

Efficiency of Light-Absorbing Films for Optoacoustic Transmitter Applications, in: Proc. SPIE 7899, Photons Plus Ultrasound Imaging Sens. 2011, 2011: pp. 789940-789940–6. doi:10.1117/12.875743.

[33] T. Buma, M. Spisar, M. O'Donnell, High-frequency ultrasound array element using thermoelastic expansion in an elastomeric film, Appl. Phys. Lett. 79 (2001) 548. doi:10.1063/1.1388027.

[34] E. Biagi, F. Margheri, D. Menichelli, Efficient laser-ultrasound generation by using heavily absorbing films as targets, IEEE Trans. Ultrason. Ferroelectr. Freq. Control. 48 (2001) 1669–1680. doi:10.1109/58.971720.

[35] S. Noimark, R.J. Colchester, B.J. Blackburn, E.Z. Zhang, E.J. Alles, S. Ourselin, P.C. Beard, I. Papakonstantinou, I.P. Parkin, A.E. Desjardins, Carbon-Nanotube-PDMS Composite Coatings on Optical Fibers for All-Optical Ultrasound Imaging, Adv. Funct. Mater. (2016) 1–7. doi:10.1002/adfm.201601337.

[36] W.Y. Chang, W. Huang, J. Kim, S. Li, X. Jiang, Candle soot nanoparticles-polydimethylsiloxane composites for laser ultrasound transducers, Appl. Phys. Lett. 107 (2015) 1–5. doi:10.1063/1.4934587.

[37] B.-Y. Hsieh, J. Kim, J. Zhu, S. Li, X. Zhang, X. Jiang, A laser ultrasound transducer using carbon nanofibers–polydimethylsiloxane composite thin film, Appl. Phys. Lett. 106 (2015) 021902. doi:10.1063/1.4905659.

[38] E. Vannacci, L. Belsito, F. Mancarella, M. Ferri, G.P. Veronese, A. Roncaglia, E. Biagi, Miniaturized fiber-optic ultrasound probes for endoscopic tissue analysis by micro-opto-mechanical technology., Biomed. Microdevices. 16 (2014) 415–26. doi:10.1007/s10544-014-9844-6.

[39] R.J. Colchester, C.A. Mosse, D.S. Bhachu, J.C. Bear, C.J. Carmalt, I.P. Parkin, B.E. Treeby, I. Papakonstantinou, A.E. Desjardins, Laser-generated ultrasound with optical fibres using functionalised carbon nanotube composite coatings, Appl. Phys. Lett. 104 (2014) 173502. doi:10.1063/1.4873678.

[40] M.A. Park, S.H. Lee, J.J. Yoh, Characterization of laser-induced ultrasound signal by reduced graphene oxide thickness and laser intensity, Appl. Phys. B Lasers Opt. 113 (2013) 389–393. doi:10.1007/s00340-013-5475-5.

[41] S. Hwan Lee, M.A. Park, J.J. Yoh, H. Song, E. Yun Jang, Y. Hyup Kim, S. Kang, Y. Seop Yoon, Reduced graphene oxide coated thin aluminum film as an optoacoustic transmitter for high pressure and high frequency ultrasound generation, Appl. Phys. Lett. 101 (2012) 2010–2014. doi:10.1063/1.4772498.

[42] H.W. Baac, J. Frampton, J.G. Ok, S. Takayama, L.J. Guo, Localized micro-scale disruption of cells using laser-generated focused ultrasound, J. Biophotonics. 6 (2013) 905–910. doi:10.1002/jbio.201200247.

[43] X. Zou, N. Wu, Y. Tian, X. Wang, Broadband miniature fiber optic ultrasound generator., Opt. Express. 22 (2014) 18119–27. doi:10.1364/OE.22.018119.

[44] Y. Tian, N. Wu, X. Zou, H. Felemban, C. Cao, X. Wang, Fiber-optic ultrasound generator using periodic gold nanopores fabricated by a focused ion beam, Opt. Eng. 52 (2013) 065005. doi:10.1117/1.OE.52.6.065005.

[45] H. Won Baac, J.G. Ok, H.J. Park, T. Ling, S.-L. Chen, a J. Hart, L.J. Guo, Carbon nanotube composite optoacoustic transmitters for strong and high frequency ultrasound generation., Appl. Phys. Lett. 97 (2010) 234104. doi:10.1063/1.3522833.

[46] Y. Hou, J.S. Kim, S. Ashkenazi, S.W. Huang, L.J. Guo, M. O'Donnell, M. O'Donnell,

Broadband all-optical ultrasound transducers, Appl. Phys. Lett. 91 (2007) 64370F–9. doi:10.1063/1.2771058.

[47] T. Buma, M. Spisar, M. O'Donnell, A high-frequency, 2-D array element using thermoelastic expansion in PDMS, IEEE Trans. Ultrason. Ferroelectr. Freq. Control. 50 (2003) 1161–1176. doi:10.1109/TUFFC.2003.1235327.

[48] S. Link, M. a El-Sayed, Shape and size dependence of radiative, non-radiative and photothermal properties of gold nanocrystals, Int. Rev. Phys. Chem. 19 (2000) 409–453. doi:10.1080/01442350050034180.

[49] G.A. Rance, D.H. Marsh, R.J. Nicholas, A.N. Khlobystov, UV-vis absorption spectroscopy of carbon nanotubes: Relationship between the ??-electron plasmon and nanotube diameter, Chem. Phys. Lett. 493 (2010) 19–23. doi:10.1016/j.cplett.2010.05.012.

[50] E. Theocharous, C.J. Chunnilall, R. Mole, D. Gibbs, N. Fox, N. Shang, G. Howlett, B. Jensen, R. Taylor, J.R. Reveles, O.B. Harris, N. Ahmed, The partial space qualification of a vertically aligned carbon nanotube coating on aluminium substrates for EO applications., Opt. Express. 22 (2014) 7290–307. doi:10.1364/OE.22.007290.

[51] B. Zeqiri, A.D. Bond, The Influence of Wave-Form Distortion on Hydrophone Spatial-Averaging Corrections - Theory and Measurement, J. Acoust. Soc. Am. 92 (1992) 1809–1821. doi:10.1121/1.403837.

[52] E.G. Radulescu, P.A. Lewin, A. Nowicki, 1-60 MHz measurements in focused acoustic fields using spatial averaging corrections, Ultrasonics. 40 (2002) 497–501. doi:10.1016/S0041-624X(02)00166-X.

[53] M.P. Cooling, V.F. Humphrey, V. Wilkens, Hydrophone area-averaging correction factors

in nonlinearly generated ultrasonic beams, J. Phys. Conf. Ser. 279 (2011). doi:10.1088/1742-6596/279/1/012002.

[54] P.N. Gélat, R.C. Preston, A. Hurrell, A theoretical model describing the transfer characteristics of a membrane hydrophone and validation, Ultrasonics. 43 (2005) 331–341. doi:10.1016/j.ultras.2004.08.003.

[55] K. Wear, Y. Liu, P. Gammell, S. Maruvada, G. Harris, Correction for frequency-dependent hydrophone response to nonlinear pressure waves using complex deconvolution and rarefactional filtering: Application with fiber optic hydrophones, IEEE Trans. Ultrason. Ferroelectr. Freq. Control. 62 (2015) 152–164. doi:10.1109/TUFFC.2014.006578.

[56] S. Eichstädt, V. Wilkens, A. Dienstfrey, P. Hale, B. Hughes, C. Jarvis, On challenges in the uncertainty evaluation for time-dependent measurements, Metrologia. 53 (2016) S125–S135. doi:10.1088/0026-1394/53/4/S125.

[57] S. Eichstädt, V. Wilkens, Evaluation of uncertainty for regularized deconvolution: A case study in hydrophone measurements, J. Acoust. Soc. Am. 141 (2017) 4155–4167. doi:10.1121/1.4983827.

[58] S. Rajagopal, T. Sainsbury, B. Treeby, B. Cox, Laser generated ultrasound sources using polymer nanocomposites for high frequency metrology, in: 2017 IEEE Int. Ultrason. Symp., IEEE, 2017: pp. 1–1. doi:10.1109/ULTSYM.2017.8091730.

[59] Araldite LY 564, Mouldlife. (2018). http://www.mouldlife.net/ekmps/shops/mouldlife/resources/Other/araldite-ly564-aradur-2954-eur-e-1-.pdf (accessed January 10, 2018).

[60] Properties of polymers, Kaye Laby Online. (2018).

http://www.kayelaby.npl.co.uk/chemistry/3_11/3_11_1.html (accessed January 10, 2018).

[61] Sylgard® 184, Dow Corning. (2018). http://www.dowcorning.com/DataFiles/090276fe80190b08.pdf (accessed January 10, 2018).

[62] G. Paltauf, P.E. Dyer, Photomechanical processes and effects in ablation., Chem. Rev. 103 (2003) 487–518. doi:10.1021/cr010436c.

[63] A. Vogel, V. Venugopalan, Mechanisms of pulsed laser ablation of biological tissues, Chem. Rev. 103 (2003) 577–644. doi:10.1021/cr010379n.

[64] T.J. Allen, B.T. Cox, P.C. Beard, Generating photoacoustic signals using high-peak power pulsed laser diodes, (2005) 233. doi:10.1117/12.597321.

[65] H.W. Baac, J.G. Ok, A. Maxwell, K.-T. Lee, Y.-C. Chen, a J. Hart, Z. Xu, E. Yoon, L.J. Guo, Carbon-nanotube optoacoustic lens for focused ultrasound generation and high-precision targeted therapy., Sci. Rep. 2 (2012) 989. doi:10.1038/srep00989.

[66] N. Wu, Y. Tian, X. Zou, V. Silva, A. Chery, X. Wang, High-efficiency optical ultrasound generation using one-pot synthesized polydimethylsiloxane-gold nanoparticle nanocomposite, J. Opt. Soc. Am. B. 29 (2012) 2016. doi:10.1364/JOSAB.29.002016.

[67] B.E. Treeby, B.T. Cox, k-Wave: MATLAB toolbox for the simulation and reconstruction of photoacoustic wave fields., J. Biomed. Opt. 15 (2010) 021314. http://www.ncbi.nlm.nih.gov/pubmed/20459236 (accessed December 10, 2014).

[68] B.E. Treeby, J. Jaros, A.P. Rendell, B.T. Cox, Modeling nonlinear ultrasound propagation in heterogeneous media with power law absorption using a k-space pseudospectral method., J. Acoust. Soc. Am. 131 (2012) 4324–36. doi:10.1121/1.4712021.

[69] B.E. Treeby, B.T. Cox, Modeling power law absorption and dispersion for acoustic

propagation using the fractional Laplacian., J. Acoust. Soc. Am. 127 (2010) 2741–48. doi:10.1121/1.3377056.

[70] M. Brio, G. Webb, A. Zakharian, Numerical Time-Dependent Partial Differential Equations for Scientists and Engineers, Elsevier, Burlington, 2010.

[71] Specific heat capacities, Kaye Laby Online. (2018). http://www.kayelaby.npl.co.uk/general_physics/2_3/2_3_6.html (accessed January 12, 2018).

[72] H. Wang, T. Ritter, W. Cao, K.K. Shung, High frequency properties of passive materials for ultrasonic transducers, IEEE Trans. Ultrason. Ferroelectr. Freq. Control. 48 (2001) 78–84. doi:10.1109/58.895911.

[73] M. Li, Z. Wang, Q. Liu, S. Wang, Y. Gu, Y. Li, Z. Zhang, Carbon nanotube film/epoxy composites with high strength and toughness, Polym. Compos. 38 (2017) 588–596. doi:10.1002/pc.23617.

[74] Densities, Kaye Laby Online. (2018). http://www.kayelaby.npl.co.uk/general_physics/2_2/2_2_1.html (accessed January 12, 2018).

[75] The speed and attenuation of sound, Kaye Laby Online. (2018). http://www.kayelaby.npl.co.uk/general_physics/2_4/2_4_1.html (accessed January 12, 2018).

[76] See supplementary material at [URL will be inserted by AIP] for animations of the illustrated wave shape transformation caused by cumulative acoustic nonlinearity, Fig. 9." SuppPub1.pptx